Supporting Information

Ihms et al. 10.1073/pnas.1315281111

SI Materials and Methods

Isothermal Titration Calorimetry. Concentrated *trp* RNA-binding attenuation protein (TRAP) and anti-TRAP (AT) stock solutions were dialyzed extensively against sample buffer (50 mM sodium phosphate, 100 mM NaCl, 0.5 mM tryptophan, 0.02% NaN_3) at pH 7 or 8. Titrations were carried out on an iTC200 system (GE Healthcare) using 30 injections (1.5 µL), except for the first injection, which was 0.5 µL. Data were analyzed using the software package Origin V.7 (OriginLab) and fit using the built-in single-site binding model provided by Microcal.

Analytical Ultracentrifugation. The predicted hydrodynamic properties of putative TRAP+AT complexes were calculated with HYDROPRO (1) on all-atom models built from available crystal structures. The effect of the six unstructured N-terminal residues of TRAP upon the calculated sedimentation coefficients was assessed by modeling and was determined to be negligible. $TRAP_{11}$-nAT_3 complexes were modeled by superimposing a fragment of the $TRAP_{12}+6AT_3$ complex structure [Protein Data Bank (PDB) ID code 2ZP8] containing one AT_3 and the two contacting TRAP protomers onto adjacent protomers of the $TRAP_{11}$ crystal structure (PDB ID code 1WAP). The translational and rotational matrices necessary to place AT_3 at each potential TRAP binding site then were obtained by superimposing free AT_3 (PDB ID code 2KO8) on the AT portion of the hybrid AT_3+TRAP_{11} coordinates using University of California, San Francisco (UCSF) Chimera (2).

Small-Angle X-Ray Scattering. Envelope densities used in the figures were visualized in UCSF Chimera with SITUS density maps generated from the averaged bead models by pdb2vol (3) using a voxel spacing of 6 Å and Gaussian smoothing at a half-radius of 6 Å.

Comparative fitting of experimental small-angle X-ray scattering (SAXS) profiles was achieved by calculating the predicted scattering profiles of putative TRAP-AT structures built from the averaged GASBOR models arranged using the transformation matrices obtained previously. For fits derived from complexes containing only a single TRAP molecule, the transformation matrices were used to build all potential unique and sterically unhindered $TRAP_{11}+1–5AT_3$ complex structures (18 total) from the averaged GASBOR envelopes of the components. Subsequently, CRYSOL was used to calculate their predicted scattering curves, which, along with the regularized scattering curves for free $TRAP_{11}$ and AT_3, were compiled into a form factor input file for OLIGOMER (4). OLIGOMER implements a nonnegative least-squares method to determine the volume fractions for possible components in experimental data. For fits obtained from complexes containing multiple TRAP molecules, a library of complex scattering curves was built in a manner similar to that described above. Fitting then was performed using a custom software program based on the minimal ensemble method used by EOM (5) and BILBOMD (6).

NMR. Comparison ^1H-^{15}N heteronuclear single quantum coherence (HSQC) NMR spectra of AT and *N*-formyl AT (*f*AT) were obtained by expression of AT in minimal medium with ^{15}N-ammonium as the sole nitrogen source and purified as previously described (7). A native control spectrum was obtained on the pooled AT sample after dialysis against 50 mM sodium phosphate, 100 mM NaCl, 2 mM DTT, 0.02% NaN_3, at pH 8. After acquisition, the AT and formyl-AT components present in the NMR sample were separated by denaturing reverse-phase HPLC. Fractions containing pure *f*AT were lyophilized and refolded as previously described (7), and the ^1H-^{15}N HSQC spectra of refolded formyl-AT were acquired. Both experiments were performed at 55 °C on a Bruker DRX 600 MHz spectrometer equipped with a triple-resonance inverse TXI Cryo-Probe. Data were processed in NMRPipe (8) and analyzed in NMRView (9).

Ion Mobility Mass Spectrometry. For ion mobility mass spectrometry, the instrument used a traveling wave ion mobility drift cell (10) to separate ions based on their collisional cross-section differences resulting from differences in size, shape, and charge. Mobility-separated ion packets reach the time-of-flight analyzer for m/z measurement at different drift times, generating a 2D spectrum. The ions from a single protein species display multiple peaks in the mass spectra as a continuous charge-state distribution. The masses of the species then can be determined by deconvoluting the charge-state distribution.

The experimental masses were determined from the m/z and assigned charge states by manually fitting the charge-state distribution to the lowest SD as shown in Table S1 (after the ± sign in the "Measured Mass" column). The deviations from the measured to the theoretical mass are listed in the right-most column in the table. Positive deviation of experimental mass from theoretical mass usually is caused by the noncovalent attachment of salt and buffer molecules, which can be quite heterogeneous and vary depending on experimental conditions. The assignments in the table are the most plausible stoichiometry based on the measured molecular weight. Some mass species detected experimentally may match to several possible structures.

1. Ortega A, Amorós D, García de la Torre J (2011) Prediction of hydrodynamic and other solution properties of rigid proteins from atomic- and residue-level models. *Biophys J* 101(4):892–898.
2. Pettersen EF, et al. (2004) UCSF Chimera—a visualization system for exploratory research and analysis. *J Comput Chem* 25(13):1605–1612.
3. Wriggers W (2012) Conventions and workflows for using Situs. *Acta Crystallogr D Biol Crystallogr* 68(Pt 4):344–351.
4. Konarev PV, Volkov VV, Sokolova AV, Koch MHJ, Svergun DI (2003) PRIMUS: A Windows PC-based system for small-angle scattering data analysis. *J Appl Cryst* 36(5):1277–1282.
5. Bernadó P, Mylonas E, Petoukhov MV, Blackledge M, Svergun DI (2007) Structural characterization of flexible proteins using small-angle X-ray scattering. *J Am Chem Soc* 129(17):5656–5664.
6. Pelikan M, Hura GL, Hammel M (2009) Structure and flexibility within proteins as identified through small angle X-ray scattering. *Gen Physiol Biophys* 28(2):174–189.
7. Sachleben JR, McElroy CA, Gollnick P, Foster MP (2010) Mechanism for pH-dependent gene regulation by amino-terminus-mediated homooligomerization of Bacillus subtilis anti-trp RNA-binding attenuation protein. *Proc Natl Acad Sci USA* 107(35):15385–15390.
8. Delaglio F, et al. (1995) NMRPipe: A multidimensional spectral processing system based on UNIX pipes. *J Biomol NMR* 6(3):277–293.
9. Johnson BA, Blevins RA (1994) NMR View: A computer program for the visualization and analysis of NMR data. *J Biomol NMR* 4(5):603–614.
10. Giles K, Williams JP, Campuzano I (2011) Enhancements in travelling wave ion mobility resolution. *Rapid Commun Mass Spectrom* 25(11):1559–1566.
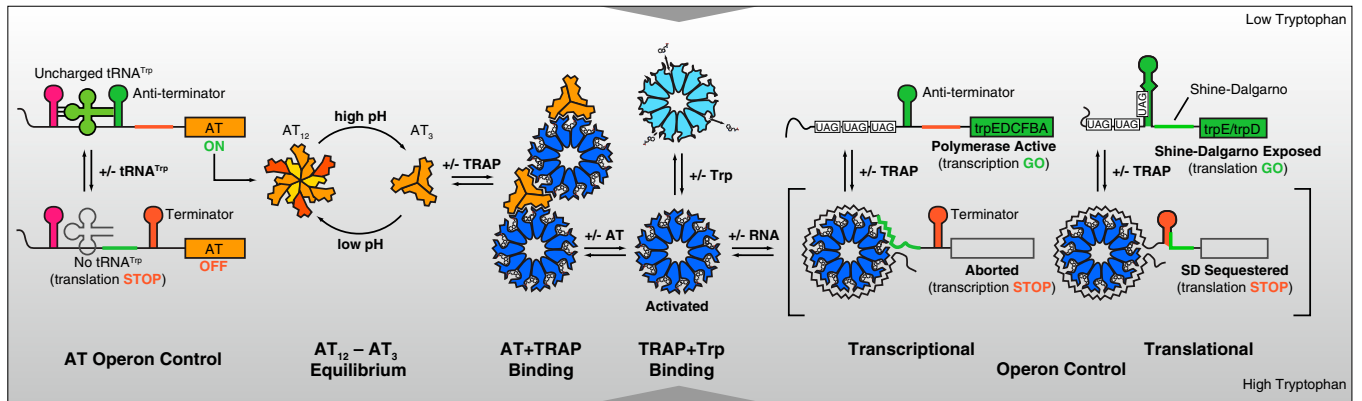
Fig. S1. Overview of the role of TRAP in regulating the *trp* operon in *Bacillus subtilis*. Undecameric TRAP directly senses the cellular concentration of tryptophan (Trp) and upon tryptophan binding is activated to bind specific sequences in the 5′-UTR of genes encoding enzymes responsible for tryptophan biosynthesis. TRAP binding results in remodeling of the RNA structure and thus can exert both transcriptional and translational-level control. TRAP can be inhibited from RNA binding by trimeric AT, which condenses together multiple TRAP rings, thereby occluding their RNA-binding surfaces. AT is up-regulated in response to accumulating uncharged tRNA^{Trp} via a translational T-box mechanism and exists in a pH-dependent equilibrium between an inactive dodecameric form, AT$_{12}$, and the TRAP-binding–competent trimeric form, AT$_3$.
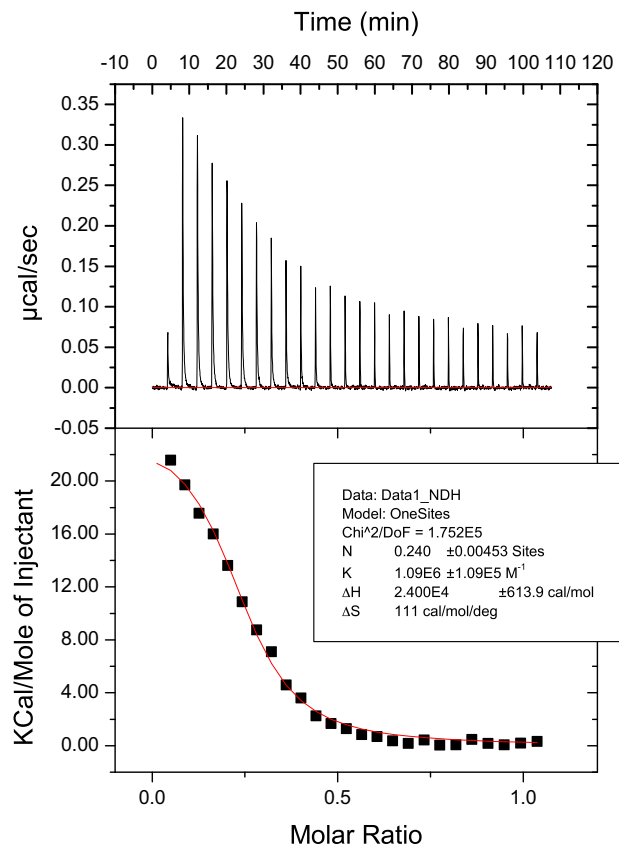
Fig. S2. Isothermal titration calorimetry shows an apparent affinity of 1 µM of TRAP for *f*AT. Representative data from titrating TRAP (1.76-mM monomer concentration) into *f*AT (0.097-mM monomer concentration) in the presence of excess (3 mM) tryptophan, at 15 °C. (*Upper*) Experimental thermogram. (*Lower*) Enthalpies per injection. The molar ratio is defined in terms of TRAP$_{11}$:AT$_3$. Integrated enthalpies are fit to a single-binding-mode model described by stoichiometry n, affinity K, and bending enthalpy ΔH. Best-fit values were 0.24 ± 0.004, 1.09 ± 0.11 × 10^6 M^{-1}, and 2.4 ± 0.6 kcal·mol^{-1}, respectively. An n value of 0.24 corresponds to an apparent stoichiometry for saturation of ~4 AT$_3$ per TRAP$_{11}$.
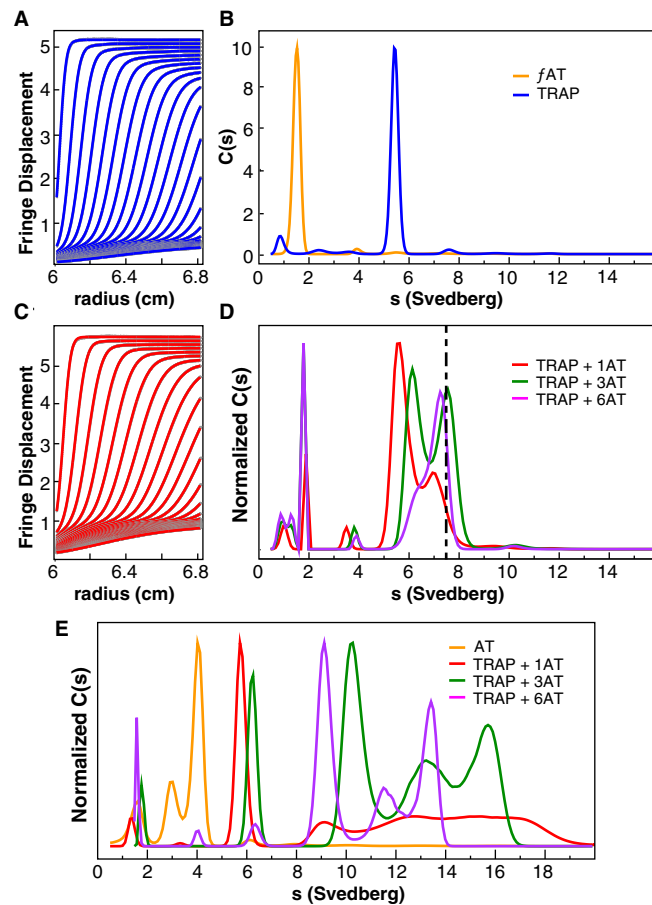
Fig. S3. Sedimentation velocity analyses of TRAP, *f*AT, and AT mixtures. (*A*) Experimental fringe displacement traces of TRAP alone (gray circles) and SEDFIT fits (blue lines) at pH 8; every 10th scan is shown. (*B*) Continuous sedimentation coefficient distributions for TRAP and *f*AT also show predominantly single sedimenting species for the components, although some formation of AT_{12} may be present at 3.9 Svedberg. (*C*) Fringe displacement traces for samples prepared with 1:1 equivalents of AT_3:$TRAP_{11}$ at pH 8 reveal significantly slower sedimenting species than at neutral pH and predominantly fewer species. Experimental data are gray circles; the SEDFIT fits are in red; every 10th scan is shown. (*D*) Sedimentation coefficient distributions for samples containing 1, 3, and 6 AT_3 per $TRAP_{11}$ at pH 8. The vertical dashed line shows the sedimentation coefficient for $TRAP_{11}$-$5AT_3$ predicted by HYDROPRO. (*E*) Sedimentation coefficient distributions for TRAP + native (deformylated AT) at pH 7.

Fig. S4. SAXS data at saturating AT conditions can be reasonably fit with single-TRAP complexes, but data at low AT:TRAP ratios cannot. (*A*) OLIGOMER fits from profiles of free AT and only single-TRAP complexes to experimental data acquired from samples at 1:1 AT_3:$TRAP_{11}$ ratios. (*Inset*) Deviation from experimental data (I_{exp}/I_{fit}) for each fit. (*B*) OLIGOMER fitting to experimental data acquired from samples containing 6:1 AT_3:$TRAP_{11}$. Discrepancies in fits at high scattering angles for both panels may arise from structural flexibility not present in the component models used to generate the TRAP-AT complexes. (*C*) All 18 possible (sterically allowed) unique $TRAP_{11}$-1–5AT_3 complex configurations assembled from the SAXS envelopes of the components generated by GASBOR.

Fig. S5. Ion mobility mass spectra of *f*AT and TRAP. (*A*) Ion mobility mass spectrum of *B. subtilis f*AT. (*B*) Ion mobility mass spectrum of *B. subtilis* TRAP-tryptophan. The formation of stacked TRAP rings has been observed previously (see text).

Table S1. Complex masses observed in ion-mobility mass spectrometry of AT and TRAP Csamples alone

	Measured mass, Da	Theoretical mass, Da	% mass error (measured − calculated), Da
$f\text{AT}_3$	$17,229 \pm 0.3$	17,229	−0.20 (−001)
TRAP_{11}	$91,858 \pm 43$	91,613	245 (0.27)
TRAP_{12}	$100,362 \pm 105$	99,942	420 (0.42)

Table S2. Complex masses observed in ion-mobility mass spectrometry of TRAP-AT mixtures

	Measured mass, Da	Possible identity	Calculated mass, Da	% mass error (measured − calculated), Da
0.5:1 AT_3:TRAP_{11}	$94,034 \pm 70$	1TRAP_{11}:11trp	93,860	174 (0.18)
	$111,760 \pm 37$	1TRAP_{11}:11trp:1AT_3	111,089	671 (0.60)
	$205,165 \pm 179$	2TRAP_{11}:22trp:1AT_3	204,948	217 (0.10)
		2TRAP_{12}:24trp*	204,785	733 (0.36)
	$205,518 \pm 43$	2TRAP_{11}:22trp:2AT_3	222,177	1,102 (0.50)
	$223,279 \pm 111$	3TRAP_{11}:33trp:1AT_3	298,808	623 (0.21)
	$299,431 \pm 48$	3TRAP_{11}:33trp:2AT_3	316,037	841 (0.27)
	$316,878 \pm 234$	2TRAP_{11}:22trp:7AT_3	308,322	1.894 (0.61)
2.0:1 AT_3:TRAP_{11}	$92,648 \pm 111$	1TRAP_{11}:11trp:1AT_3[†]	111,089	−463 (−0.42)
	$110,626 \pm 85$	1TRAP_{11}:11trp:2AT_3[†]	128,318	−67 (−0.05)
	$128,251 \pm 52$	1TRAP_{11}:11trp:3AT_3	145,547	405 (0.28)
	$145,952 \pm 67$	1TRAP_{11}:11trp:4AT_3	162,776	591 (0.36)
	$163,367 \pm 148$	1TRAP_{11}:11trp:5AT_3	180,005	406 (0.22)
	$180,411 \pm 144$	2TRAP_{12}:24trp[†]	20,785	77 (0.04)

*TRAP has been observed to form both 11- and 12-membered rings (see text).
[†]TRAP frequently loses bound tryptophan, exhibiting a lower than expected mass.